Monthly Notices
of the
ROYAL ASTRONOMICAL SOCIETY

MNRAS **524,** 351–360 (2023) https://doi.org/10.1093/mnras/stad1903
Advance Access publication 2023 June 23

The challenges of identifying Population III stars in the early Universe

Harley Katz,[1]★ Taysun Kimm ,[2] Richard S. Ellis,[3] Julien Devriendt[1] and Adrianne Slyz[1]
[1]*Sub-department of Astrophysics, University of Oxford, Keble Road, Oxford OX1 3RH, UK*
[2]*Department of Astronomy, Yonsei University, 50 Yonsei-ro, Seodaemun-gu, Seoul 03722, Republic of Korea*
[3]*Department of Physics and Astronomy, University College London, Gower Street, London WC1E 6BT, UK*

Accepted 2023 May 19. Received 2023 May 19; in original form 2022 July 10

ABSTRACT

The recent launch of *JWST* has enabled the exciting prospect of detecting the first generation of metal-free, Population III (Pop. III) stars. Determining characteristics that robustly signify Pop. III stars against other possible contaminants represents a key challenge. To this end, we run high-resolution (sub-pc) cosmological radiation hydrodynamics simulations of the region around a dwarf galaxy at $z \geq 10$ to predict the emission line signatures of the Pop. III/Pop. II transition. We show that the absence of metal emission lines is a poor diagnostic of Pop. III stars because metal-enriched galaxies can maintain low [O III] 5007 Å that may be undetectable due to sensitivity limits. Combining spectral hardness probes (e.g. He II 1640 Å/H α) with metallicity diagnostics is more likely to probe metal-free stars, although contamination from Wolf–Rayet stars, X-ray binaries, or black holes may be important. The hard emission from Pop. III galaxies fades fast due to the short stellar lifetimes of massive stars, which could further inhibit detection. Pop. III stars may be identifiable after they evolve off the main sequence due to the cooling radiation from nebular gas or a supernova remnant; however, these signatures are also short-lived (i.e. few Myr). Contaminants including flickering black holes might confuse this diagnostic. While *JWST* will provide a unique opportunity to spectroscopically probe the nature of the earliest galaxies, both the short time-scales associated with pristine systems and ambiguities in interpreting emission lines may hinder progress. Special care will be needed before claiming the discovery of systems with pure Pop. III stars.

Key words: stars: formation – stars: Population III – galaxies: evolution – galaxies: formation – galaxies: high-redshift.

1 INTRODUCTION

One of the most compelling scientific goals of the *JWST* is either detecting or placing strong constraints on the properties of the first generation of metal-free, Population III (Pop. III) stars (Gardner et al. 2006). Very little is known about their properties, such as when they started forming, when they stopped forming, their initial mass function (IMF), or metal yields because to date, there has yet to be a robust detection of Pop. III stars – despite there being speculation about a few peculiar objects (e.g. Sobral et al. 2015; Vanzella et al. 2020; Welch et al. 2022). The constraints we have on their characteristics are either derived from high-resolution numerical simulations (e.g. Abel, Bryan & Norman 2002; Bromm, Coppi & Larson 2002; Stacy, Greif & Bromm 2010; Greif et al. 2011; Hirano et al. 2014; Hosokawa et al. 2016) or from stellar archaeology around the Milky Way (e.g. Beers & Christlieb 2005; Frebel, Johnson & Bromm 2007; Karlsson, Bromm & Bland-Hawthorn 2013). Nevertheless, this is hopefully set to change with the recent launch of *JWST* or future facilities such as High Angular Resolution Monolithic Optical and Near-infrared Integral field spectrograph (HARMONI) on the Extremely large telescope (ELT) (Grisdale et al. 2021).

Even with optimistic assumptions on the Pop. III IMF and the redshift to which some gas in the Universe can remain pristine, it is unlikely that individual metal-free stars will be detectable with *JWST* (e.g. Zackrisson et al. 2011; Rydberg et al. 2013; Schauer, Drory & Bromm 2020). Although, prospects are better if Pop. III stars form in large groups and a significant amount of observing time is spent on lensing clusters (e.g. Stiavelli & Trenti 2010; Pawlik, Milosavljević & Bromm 2011; Jeon & Bromm 2019; Vikaeus et al. 2022). Direct constraints on the Pop. III IMF may also arise from observing their supernovae, if they happen to be particularly bright, or result in a gamma-ray burst (Lazar & Bromm 2022).

One of the primary issues with robustly detecting Pop. III stars is determining the spectral signatures that differentiate them from other classes of objects that form in the early Universe. Such contaminants could include direct collapse black holes or a second generation of already metal enriched stars (Nakajima & Maiolino 2022). Due to their possible higher masses and metal-free nature, the spectra of Pop. III stars are expected to be considerably harder than their Pop. II counterparts (e.g. Schaerer 2002). For this reason, it has been postulated that spectral signatures from high-energy ionization states (e.g. He II; Oh, Haiman & Rees 2001; Tumlinson, Giroux & Shull 2001) represent one possible indirect signature of Pop. III stars. However, strong He II lines by themselves are not a definitive signature of metal-free stars because other sources, such as Wolf–Rayet stars, X-ray binaries, or black holes can similarly produce strong He II emission (e.g. Erb et al. 2010; Inoue 2011; Schaerer, Fragos & Izotov 2019; Nakajima & Maiolino 2022). Pop. III stars are also predicted to excite strong hydrogen emission lines

---

★ E-mail: harley.katz@physics.ox.ac.uk

such as Ly α, H α, and H β, although the former is unlikely to be detectable due to the optically thick intergalactic medium (IGM) at high redshifts (Gunn & Peterson 1965; Inoue et al. 2014). Another possible contaminant are galaxies that have metals but the metal emission lines are simply too weak to be detected.

Given the recent launch of *JWST*, it is timely to revisit the spectral signatures of Pop. III stars in the context of fully coupled radiation hydrodynamics simulations that resolve much of the physics driving emission lines. While there is a rich literature on the formation of Pop. III stars in cosmological simulations (e.g. Abel et al. 2002; Bromm et al. 2002; O'Shea & Norman 2007), the new aspect of this work is that here we focus specifically on using a non-equilibrium chemistry network for primordial species, metals, and molecules to directly predict the emission line signatures of the Pop. III–Pop. II transition. This provides a complementary view to the various photoionization models that have been analysed on this topic (e.g. Inoue 2011; Nakajima & Maiolino 2022).

2 METHODS

For this work, we employ high-resolution cosmological radiation hydrodynamics simulations run with the RAMSES-RTZ code (Katz 2022), an extension of the RAMSES-RT code (Teyssier 2002; Rosdahl et al. 2013; Rosdahl & Teyssier 2015) that includes modules for radiation-coupled H_2 (Katz et al. 2017) and metal chemistry (Katz 2022). The underlying physics closely follows that presented in Kimm et al. (2017) and here we briefly highlight the features included in the simulation with a particular emphasis on the changes made for these runs.

The simulations follow gravity, hydrodynamics, radiation transfer, and various chemistry, cooling, and heating processes. The radiation is followed in eight frequency bins (see table 2 in Kimm et al. 2017), spanning from the infrared (IR; for multiscattered radiation pressure) through He II ionizing photons, using the M1 method (Levermore 1984). To reduce the computational cost of the RT, we employ a reduced speed of light approximation, adopting $c_{\rm sim} = 0.01c$.[1] The radiation is coupled to the gas via photoionization, photoheating, and radiation pressure (both direct ultraviolet and multiscattered IR). Similar to Kimm et al. (2017) we follow H I, H II, e, He I, He II, and He III, but new for this work, we also follow various ionization states of O I–VIII, C I–VI, N I–VII, Fe I–VI, Si I–VI, S I–VI, Ne I–VI, and Mg I–VI. Atomic data for each metal closely follows that adopted by CLOUDY v.17 (Ferland et al. 2017). Cooling for primordial species follows the methods presented in Rosdahl et al. (2013) and Katz et al. (2017) and cooling for metals is calculated at low temperatures ($T < 10^4$ K) by computing the equilibrium level populations of certain ions and for high temperatures ($T \geq 10^4$ K) by using look-up tables (see Oppenheimer & Schaye 2013; Katz 2022).

Cosmological initial conditions are generated for a halo with mass $\sim 3 \times 10^8$ M$_\odot$ at $z = 10$ in a volume of 5^3 cMpc^3 using MUSIC (Hahn & Abel 2011), assuming the following cosmology: $\Omega_{\rm m} = 0.311$, $\Omega_{\rm b} = 0.045$, $\Omega_\Lambda = 0.689$, and $h = 0.6766$ (Planck Collaboration VI 2020). Due to the large computational expense of these simulations, we apply the zoom-in technique and place the bulk of our resolution elements around a single galaxy, ensuring that there is no contamination from low-resolution elements within the virial radius at any point. The base grid of the simulation is initialized on level 7 (128^3). The dark matter particle mass within the high resolution region (level 11, initially representing 1 per cent of the computational volume) is 492 M$_\odot$, corresponding to an effective resolution of 2048^3. Throughout the course of the simulation, we allow the adaptive mesh to refine when either the Jeans length is not resolved by at least eight cells, or the dark matter or gas mass of the cell grows to eight times its initial value. The minimum cell size is 0.8 pc at $z = 10$ and remains constant in comoving coordinates (resulting in even smaller cell sizes at higher redshifts).

When the gas becomes dense enough, star particles are allowed to form. This occurs when the turbulent Jeans length is unresolved (see e.g. Kimm et al. 2017) and the gas is converging on a local density maximum. If these criteria are satisfied, star formation proceeds in two different modes depending on metallicity. Pop. III stars can form when the gas metallicity is $< 10^{-6}$ Z$_\odot$, while Pop. II stars form at higher metallicities. In the case of Pop. II stars, particle masses are integer multiples of 500 M$_\odot$. The number of star particles formed is drawn from a Poisson distribution with the conversion rate calculated via a Schmidt law (Schmidt 1959). The efficiency of conversion depends on the thermo-turbulent properties of the gas calibrated on high-resolution molecular cloud simulations (Padoan & Nordlund 2011; Federrath & Klessen 2012). While these simulations were not run at the metallicities that we probe in this work, both Federrath & Klessen (2012) and Glover & Clark (2012) argue that star formation rates (SFRs) in simulated clouds have little sensitivity to metallicity. Pop. II star particles are assumed to host stellar populations that follow a Kroupa IMF (Kroupa 2001). In the case of Pop. III stars, when the star formation criteria are met, we draw individual star particle masses from a stellar IMF using the functional form from Wise et al. (2012a):

$$\frac{{\rm d}N}{{\rm d}\log M} \propto M^{-1.3} \exp\left[-\left(\frac{M_{\rm char}}{M}\right)^{1.6}\right], \tag{1}$$

assuming a characteristic mass $M_{\rm char} = 100$ M$_\odot$ (e.g. Hirano et al. 2014; Kimm et al. 2017).

Star particles impact their environment in numerous ways. During the course of their lifetime, they inject photons into their host cells. For Pop. III stars, we adopt the age- and mass-dependent spectral energy distributions (SEDs) from Schaerer (2002) and for Pop. II stars, we use the age, mass, and metallicity[2] dependent SEDs from BPASS v.2.2.1 (Stanway & Eldridge 2018). When Pop. III stars reach the end of their lifetime, they can either explode via supernova (SN) or directly collapse to a black hole. The energy per Pop. III SN and the mass ranges for SN versus direct collapse are adopted from Wise et al. (2012a), which are based on Woosley & Weaver (1995), Heger & Woosley (2002), and Nomoto et al. (2006; see equations 22 and 23 of Kimm et al. 2017). For Pop. II stars, we follow both Type II core–collapse SN as well as SNIa. We randomly sample the stellar IMF to determine when to inject core–collapse SN following the age–mass distribution of Raiteri, Villata & Navarro (1996). When SN occur, momentum is injected into the simulations following the mechanical feedback model of Kimm et al. (2015). Stellar winds from asymptotic giant branch (AGB) stars are also included using the method presented in Agertz et al. (2013).

During all of these energetic feedback processes, metals are released into the gas. In all cases, yields are dependent on stellar

---

[1] While non-ionizing radiation is expected to propagate faster than this, as we show below, star formation is incredibly short lived and is not sustained at any significant level until $z \sim 10$, at which point the simulation is stopped. Thus, we expect any long-range interactions to be minor.

[2] For Pop. II star particles in the simulation with metallicities lower than the range sampled in BPASS (0.0005 Z$_\odot$), we assume the lowest metallicity SED in BPASS applies.

mass. For Pop. III stars, we consider individual SN yields from typical Type II SN (Nomoto et al. 2006), hypernova (Nomoto et al. 2006), and pair-instability SN (PISN; Heger & Woosley 2002). The mass thresholds for each are described in Kimm et al. (2017). Metal yields for Pop. II core–collapse SN are adopted from Portinari, Chiosi & Bressan (1998), while SNIa yields are from Seitenzahl et al. (2013). Finally, AGB wind yields are from Pignatari et al. (2016). We follow the enrichment of O, N, C, Mg, Si, S, Fe, Ne, and Ca.

To analyse the simulations, we use the AMIGA halo finder to identify the dark matter haloes (Gill, Knebe & Gibson 2004; Knollmann & Knebe 2009) using the virial overdensity criteria of Bryan & Norman (1998). For each halo, we compute the luminosities of various emission lines. Line emission from primordial species is computed following the fitting functions presented in Katz et al. (2022) including emission from both recombination and collisional emission, while metal emission line luminosities are calculated with PYNEB (Luridiana, Morisset & Shaw 2015) assuming only collisional emission. Due to the very low metallicities, we neglect the impact of dust on the presented emission line luminosities. This assumption should hold in a model where the dust-to-gas mass ratio scales as a power law with metallicity (e.g. Rémy-Ruyer et al. 2014).

3 RESULTS

The two primary questions that we would like to address with our simulations are: What are the spectral features that differentiate Pop. III star formation from metal enriched stellar populations and are these signatures detectable? In this section, we describe the general properties of the simulated galaxy population, discuss the spectral features of these simulated galaxies, and comment on the complexities of identifying a true Pop. III star or galaxy with observations.

3.1 High-redshift galaxy properties

The simulation follows the formation and evolution of the region around a halo with mass $\sim 3 \times 10^8$ M$_\odot$ by $z = 10$. We study the population of haloes inside the high resolution Lagrange region of the main halo. The region contains 356 uncontaminated dark matter haloes with at least 300 particles (21 of which are host stars). In Fig. 1, we show maps of dark matter, gas, and oxygen, as well as a zoomed in distribution of O I, O II, and O III at $z = 10$. At this redshift, the main halo has recently undergone a major merger (a relatively common event at high redshift). There is a significant gas concentration at the centre of the halo and a repeated series of star formation and SN events have enriched a large fraction of the volume with oxygen, some of which has escaped the halo, into the IGM. The structure in the centre of the halo is highly complex and filled with various ionization states of oxygen, dictated by both the local radiation field, SN feedback, and the presence of shocks.

More quantitatively, the first Pop. III stars formed at $z \sim 18$. This can be seen in the top panel of Fig. 2, where we show the SFR as a function of time within the Lagrange region, split between Pop. III and Pop. II star formation. Due to the fact that not all Pop. III stars explode via SN, the first metal enrichment does not occur until $z \sim 16.5$. This can be seen as the spike in the O, C, and Fe abundances in the bottom panel of Fig. 2. The first SN increases the mass-weighted metallicity of the system up to 10^{-4} Z$_\odot$ in O and Fe and 10^{-5} Z$_\odot$ in C. The exact enrichment levels for each metal are highly dependent on the mass of the Pop. III stars that explode. We expect this to vary between haloes at high redshift because the yields depend both on the mass of the star and the type of SN (see Heger & Woosley 2002; Nomoto et al. 2006 for the magnitude of these variations).

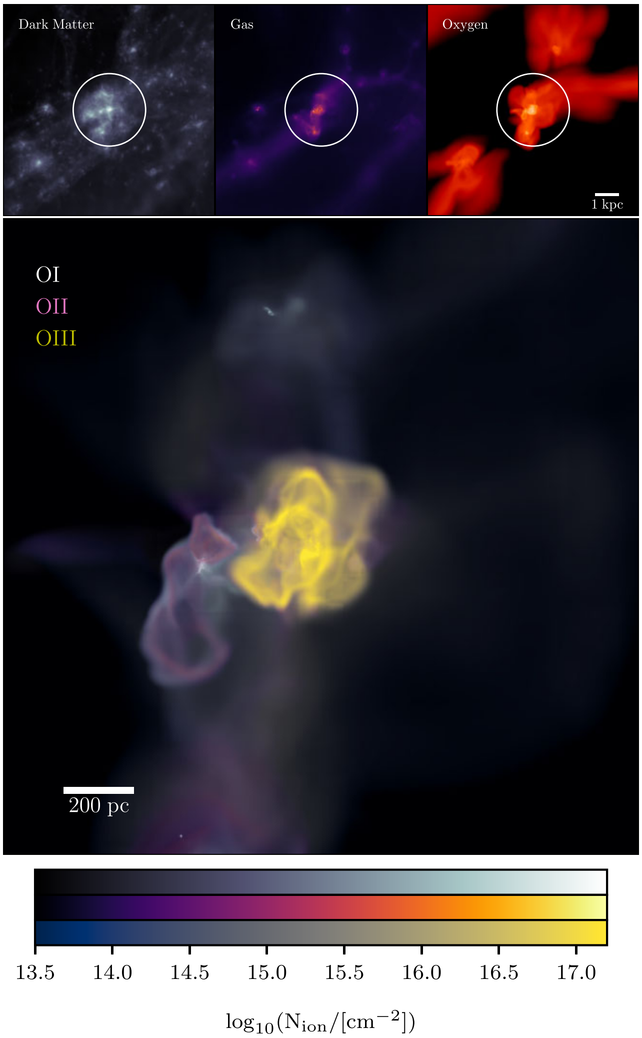

Figure 1. Top: Surface density maps of dark matter, gas, and oxygen in the simulation at $z = 10$. The white circle shows the virial radius (1.72 kpc) of the most massive halo in the simulation. Bottom: Map of O I, O II, and O III column density (as shown in the colour bar) in the central regions of the most massive halo.

Once the region becomes metal enriched, Pop. II star formation can proceed. This is shown as the magenta line in the top panel of Fig. 2. There is a delay between when the first SN explode ($z \sim 16.5$) and when Pop. II stars form ($z < 15$) due to the fact that the gas has to resettle in the halo that hosted the SN, and for the metals that escaped the halo, it takes time for them to be accreted onto neighbouring systems. A mixed mode of Pop. III and Pop. II star formation continues until $z \sim 11$. By this time, the mass-weighted metallicity has increased by about a factor of three, at which point star formation is completely dominated by Pop. II stars. We note that the exact length of the mixed-mode epoch and the redshift at which the Pop. II-dominant epoch begins are sensitive to both the individual histories of each halo and our definition for the metallicity threshold that separates Pop. II and Pop. III stars. If we adopted a higher metallicity threshold, the results here may change. This issue is further discussed below.

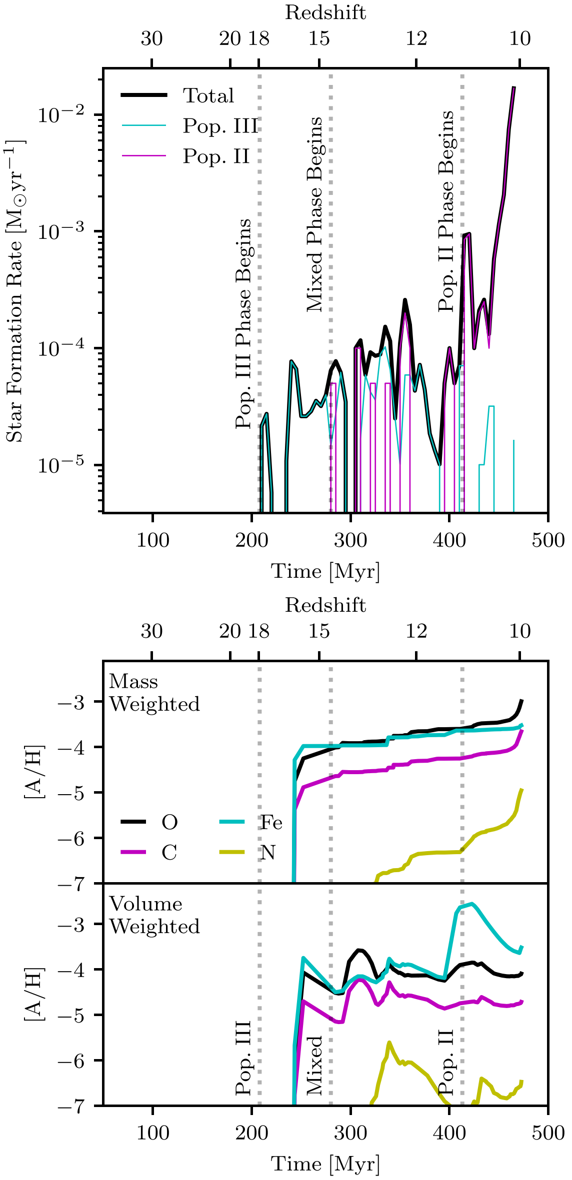

Figure 2. Top: SFR for the 21 star-forming haloes in the Lagrange volume as a function of time (black) split between the contribution of Pop. III stars (cyan) and Pop. II stars (magenta). Bottom: Mass-weighted or volume-weighted metallicities of individual elements (O, C, Fe, and N) as a function of time.

Slightly before $z = 10$, the halo undergoes a major merger that results in a steep increase in star formation and metal enrichment. By comparing the mass-weighted and volume-weighted gas metallicities in the Lagrange volume, we can analyse the enrichment of the ISM versus the IGM. While the mass-weighted metallicity continuously rises with decreasing redshift, the evolution of volume-weighted metallicity is more complex and sensitive to gas inflowing into the Lagrange region and the ability for stars to eject metals from the haloes. In general, the volume-weighted metallicity remains below the mass-weighted values suggesting that the metals are more concentrated in the haloes rather than in the IGM.

In the absence of heavy elements, H_2 is the primary coolant of the ISM. In Fig. 3, we show the evolution of total masses of H_2, C II (one of the dominant coolants at higher metallicity), and CO[3] (one of the dominant coolants at high density and high metallicity). At $z \geq 16.5$, a baseline level of H_2 is formed via reactions with H^-. Once the first metals are released into the ISM and IGM, C II can form as well and simultaneously the main-mode of H_2 formation transitions from the primordial channel to formation on dust. Future telescopes such as ngVLA will provide the opportunity to detect C II in the redshift interval $15 \lesssim z \lesssim 20$, which may help probe the properties of the first stars (Carilli et al. 2018). CO is also detectable at high redshift with the ngVLA, which could also be interesting for placing constraints on the properties of the first stars; however, we find the amount of CO remains limited until sufficient self-shielding can occur in the ISM. Due to the small size of the halo and the limited amount of CO formation, emission from CO is unlikely to be observable in such environments, even with next-generation telescopes. Nevertheless, more massive haloes will remain exciting targets for molecular gas studies at high redshift.

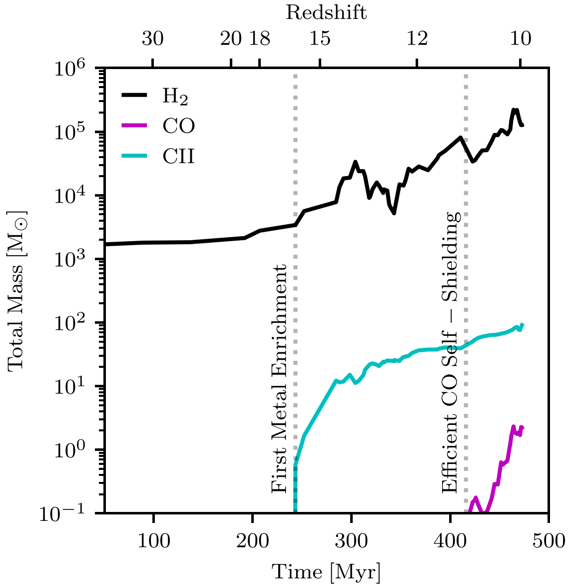

Figure 3. Evolution of the total mass of H_2 (black), C II (cyan), and CO (magenta) within the Lagrange region of the main halo as a function of time.

Having described the star formation, metal enrichment, and molecular properties of the gas in the simulation, we continue our analysis by studying the spectral features of the simulated galaxies.

3.2 The absence of metallic emission lines

As Pop. III stars are by definition metal-free, their star forming clouds are also expected to be of pristine, primordial composition. The observation of a galaxy with strong He II 1640 Å, H α, and H β emission with no metal emission lines is potentially a signature of Pop. III stars (Schaerer 2002; Raiter, Schaerer & Fosbury 2010; Inoue 2011). From an observational perspective, the absence of metal emission lines will be difficult to prove because the finite integration times and sensitivity limits will only allow for upper limits on metal emission line strengths, rather than robustly proving that metal emission lines are completely absent. The key question is

---

[3] The CO abundance is calculated in equilibrium in post-processing using the model from Nelson & Langer (1997).

how strong are the metal emission lines expected to be with respect to the Balmer emission, in simulated high-redshift galaxies.

In Fig. 4, we show the flux ratios of [O III]/H β (left), [O II]/H β (centre), and [O III]/[O II] (right) for simulated galaxies in the redshift interval $10 \leq z \leq 16$ coloured by their SFR. Oxygen emission lines are expected to be the brightest metal emission lines at these epochs due to the early enrichment from core–collapse SN (e.g. Maiolino & Mannucci 2019), and the collision strengths of these particular transitions. As the metallicity decreases, [O III]/H β and [O II]/H β also decreases such that at $12 + \log_{10}\left(\frac{\mathrm{O}}{\mathrm{H}}\right) = 6$, our simulations predict flux ratios of $\sim 10^{-2}$ compared to H β. Such predictions are not unique to our simulations as CLOUDY models (see the grey lines and cyan points in Fig. 4) of primordial galaxies predict similar flux ratios (Inoue 2011; Nakajima & Maiolino 2022), respectively. Considering that our predictions are completely independent[4] of CLOUDY, it is encouraging that both methods are in reasonable agreement. However, because the simulation samples a diversity of ISM conditions and star formation histories, we do find additional scatter in our relations related to the SFR and ISM structure of the galaxy. This is because the SFR controls the number of ionizing photons, electron density, and temperature via radiative and SN feedback while the ISM structure dictates how well this feedback couples to the gas. At fixed metallicity, the simulated galaxies exhibit a wide diversity of SFRs and ISM conditions. Such effects are not captured via simple photoionization models with a fixed uniform gas density and SFR. In particular, we tend to find many galaxies that scatter below and above the [O III]/H β and [O II]/H β predictions from (Inoue 2011; Nakajima & Maiolino 2022). These are the weakest star-forming galaxies in our simulations which have the lowest ionization parameters.

For comparison, we also show the location of Green Pea galaxies (Yang et al. 2017a), Blueberry galaxies (Yang et al. 2017b), and low-metallicity, low-redshift SDSS galaxies (Izotov et al. 2019) in Fig. 4. The low-metallicity galaxies from Izotov et al. (2019) tend to have very comparable [O III]/H β, higher [O II]/H β, and slightly lower [O III]/[O II] compared to the simulated galaxies and CLOUDY models (Inoue 2011; Nakajima & Maiolino 2022). Green Peas and Blueberries tend to be at higher metallicity than the simulated galaxies (see also Katz et al. 2022).

3.3 The absence of metal emission lines with strong He II 1640 Å

Although we argue that [O III]/H β (or [O II]/H β) is, by itself, insufficient to identify a Pop. III stellar population, if we combine the [O III]/H β ratio with the He II 1640 Å/H α ratio, we do find a region of parameter space that is only populated by galaxies dominated by Pop. III stars. The red shaded region in the bottom right of Fig. 5 shows that the parameter space with [O III]/H $\beta < 10^{-1.5}$ and He II 1640 Å/H $\alpha > 10^{-0.6}$ consists of only systems with stellar populations with a high Pop. III fraction. Consistent with previous claims in the literature (e.g. Schaerer 2002), we can confirm that weak metal emission lines and strong He II 1640 Å emission is a signature of Pop. III stars in our simulations.

Within this Pop. III parameter space, we find three interesting features. There are numerous systems that have [O III]/H $\beta = 0$ (represented as downward arrows in Fig. 5). These are genuine Pop. III stars forming in pristine, zero-metallicity gas clouds. These types of systems are what is typically expected of Pop. III stars.

Next, we have a galaxy that appears as the blue point in the shaded region that hosts a stellar population that is a mix of Pop. II and Pop. III stars. Such mixes are common in our simulation, although not all have high He II 1640 Å emission. A dark matter map of this galaxy with the locations of the Pop. II and Pop. III star particles is shown in Fig. 6. These mixed systems add to the complexity of detecting a fully Pop. III-dominated galaxy. Simulations with larger volumes (e.g. Xu et al. 2016) may find similarly complex systems of this nature that potentially pollute the region of Fig. 5 that we ascribe as being Pop. III.

Going into more detail on this specific galaxy, within 100 pc of the centre, we find two Pop. III star particles of ages 98 and 124 Myr, the former of which exploded as a PISN and the latter collapsed directly into a black hole. The third star particle is a 500 $\mathrm{M}_{\odot}$ cluster of Pop. II stars with an age of 20 Myr that is driving most of the line emission. This system is surrounded (within 2 kpc) by three more Pop. III stars, one of which is 340 $\mathrm{M}_{\odot}$, with an age of 4.6 Myr, that is likely helping to drive some of the He II emission externally.

It is also important to consider that the origin of strong He II emission is unknown at low redshifts and it is possibly driven by X-ray binaries, Wolf–Rayet stars, or other sources (e.g. Erb et al. 2010; Schaerer et al. 2019). BPASS SED neglects some of these sources (e.g. X-ray binaries), so we are potentially under-predicting the He II luminosities of our Pop. II galaxies if such sources are present at high redshift. This would further pollute this diagnostic, making it more difficult to identify genuine Pop. III stars.

Finally, we find galaxies that are fully dominated by Pop. III stars but exhibit metal emission because we are observing a cooling SN remnant. Hence, the presence of metal emission lines does not necessarily rule out the system from being Pop. III, even though this cooling phase is expected to be short-lived.

More specifically, there is a galaxy that is completely dominated by Pop. III stars but has [O III]/H $\beta = 10^{-1.5}$. We show maps of the dark matter, gas, and temperature, and the surface brightness maps of He II 1640 Å, H α, and [O III] 5007 Å for this galaxy in Fig. 7. This system hosted a single 180 $\mathrm{M}_{\odot}$ Pop. III star that recently exploded as a PISN. The PISN enriched the surrounding medium with metals so the emission that is seen is a combination of the recombination emission due to photoionization from the star and the cooling radiation from the SN remnant. The interesting characteristic of this galaxy is that there is no stellar continuum. By definition (excluding the contribution from nebular continuum), the equivalent widths of all of the emission lines from this system are infinity. We discuss such systems further in Section 3.5. If another Pop. III star formed in this system before the first evolved off the main-sequence, we might expect an increase in luminosity for all emission lines, including those from metals.

3.4 Time windows for detection

If Pop. III stars were predominantly massive, their main-sequence lifetimes would be very short. Hence, the emission line signatures are also expected to be short lived (e.g. Schaerer 2002, 2003). Therefore, Pop. III lifetime is an important parameter when con-

---

[4] Note that in Katz (2022), we demonstrated that in the equilibrium limit, RAMSES-RTZ and CLOUDY yield similar ionization fractions for metal species as a verification of our numerical integrator and chemical model. Differences in emission line strengths can arise, for example, if the system is out of chemical equilibrium, due to a complex star formation history and a varying, time-dependent radiation field, changing gas conditions, or due to the different atomic data in PyNeb compared to CLOUDY.

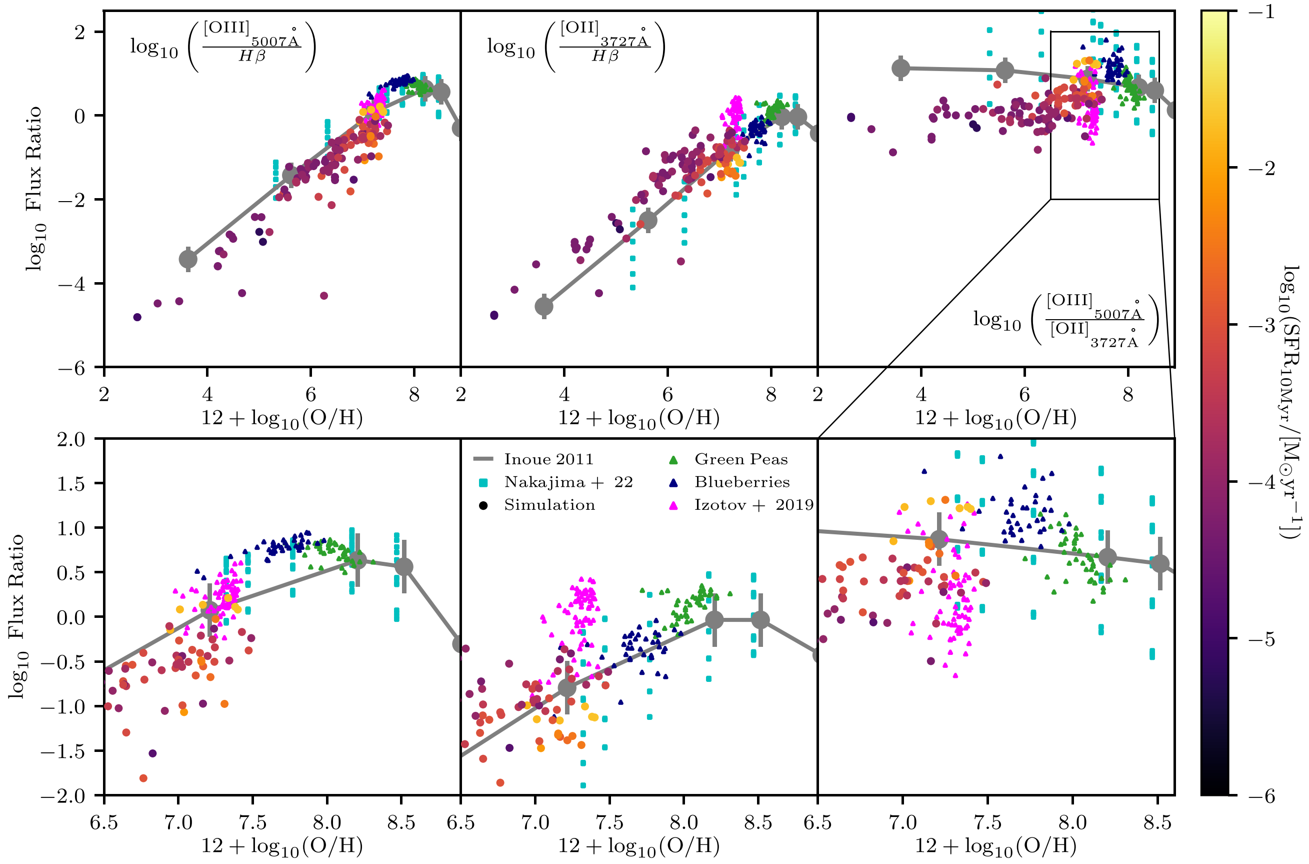

Figure 4. Flux ratios of [O III]/H β (left), [O II]/H β (centre) or [O III]/[O II] (right) for the simulated galaxy population in the redshift range $10 \leq z \leq 16$. The bottom row shows a zoomed in version of the top row. The data points from the simulation are coloured by their 10 Myr-averaged SFR. For comparison, we show results from the CLOUDY models of Inoue (2011) (grey) and Nakajima & Maiolino (2022) (cyan squares) for primordial stellar populations. Similarly, we show flux ratios for local Green Pea galaxies (Yang et al. 2017a), Blueberry galaxies (Yang et al. 2017b), and very low metallicity sloan digital sky survey (SDSS) galaxies (Izotov et al. 2019) as different coloured triangles.

sidering their detectability (Zackrisson et al. 2012; Rydberg et al. 2013).

In the top panels of Fig. 8, we show the time evolution of the He II 1640 Å, H α, and H β emission for eight haloes in the simulation as a function of time after the formation of a Pop. III star. The lines are coloured based on the initial mass[5] of the Pop. III star that formed in the halo. The luminosities have been normalized to the maximum luminosity of the line recorded after the star formation event.[6] In most cases, the He II 1640 Å fades by nearly two orders of magnitude within 5 Myr and the Balmer emission shows similar properties. This result is unsurprising given that our Pop. III stars are in general massive and we have adopted the SED of Schaerer (2002). The unique aspect of this work is that we can see how this signal fades for a realistic gas distribution. In the bottom panel of Fig. 8, we show the ratio of He II 1640 Å/H α normalized to the value of this ratio after the star formation event. In general, the He II 1640 Å emission decreases faster than H α. This explains why the Pop. III galaxies in Fig. 5 that have no metal emission lines also show weak He II 1640 Å/H α.

There is a single halo in our simulation where the He II 1640 Å emission appears to remain strong for ~10 Myr. Looking at this system in more detail, we find that a second Pop. III star formed in the galaxy very soon after the first. However, our simulation output time cadence is 9 Myr, and thus the He II 1640 Å luminosity likely drops between the formation of the first and second Pop. III star. The formation of two Pop. III stars in such quick succession is rare in our simulation, but we note that these predictions are highly IMF/model dependent. For example, in the model of Xu et al. (2016), multiple Pop. III stars commonly form in the same halo because even though they adopt the same IMF shape as used here, their characteristic mass is much lower ($40\,\mathrm{M_\odot}$ versus $100\,\mathrm{M_\odot}$).

It is important to consider that the formation of a single massive Pop. III star can enrich a galaxy up to the critical metallicity needed for Pop. II star formation in our model. There are only two Pop. III stars in our simulation with non-zero metallicity. As the galaxies become more massive, it can maintain a higher SFR and sustain bright emission line luminosities for a much longer period of time. Furthermore, our chosen Pop. II SED (BPASS) allows for ionizing photons for >10 Myr after the formation of a star particle, which represents a much longer window for detection of a single burst

---

[5] In the case where multiple Pop. III stars form, the line is coloured based on the mass of the first star to form.

[6] Note that because the simulation outputs snapshots at fixed times, there is often some delay after the formation of each star before we can first measure the emission line luminosities. The time cadence of our snapshots is often <5 Myr so we expect our curves to be reasonably time-resolved.

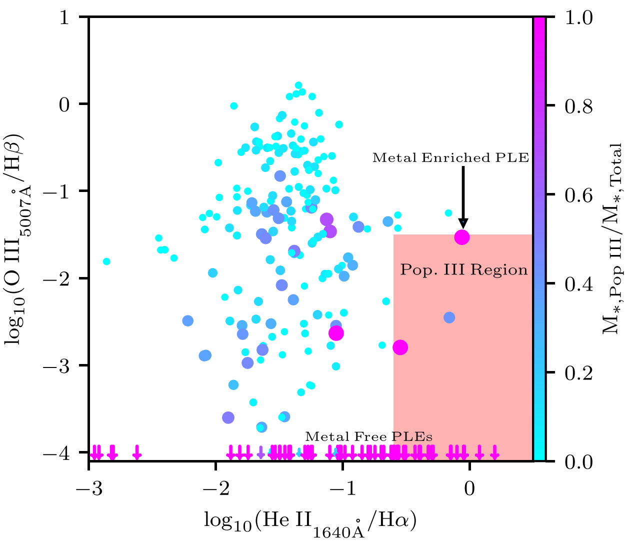

Figure 5. He II 1640 Å/H α versus [O III]/H β for simulated galaxies in the redshift range $10 \le z \le 16$ that have had star formation in the past 100 Myr and have H α luminosities $>10^{36}$ erg s^{-1}. We have coloured the points based on the fraction of the stellar population that is comprised of Pop. III stars (or their remnants). Downward arrows represent galaxies that have [O III]/H β $< 10^{-4}$. The red shaded region in the bottom right represents the parameter space where only Pop. III-dominated galaxies are found in our simulations. We have labelled the locations of the different types of pure line emitters (PLEs) as discussed in Section 3.5.

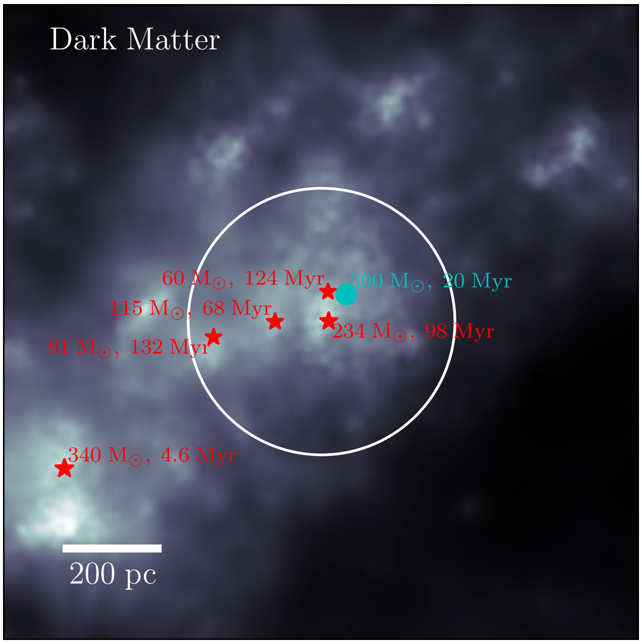

Figure 6. Dark matter map of a galaxy with mixed Pop. III and Pop. II star formation at $z = 12.6$. The red stars represent Pop. III stars and the cyan circle shows the location of a Pop. II star cluster. The ages and initial masses of each star particle are annotated on the map. The circle represents the virial radius of the halo (588 pc).

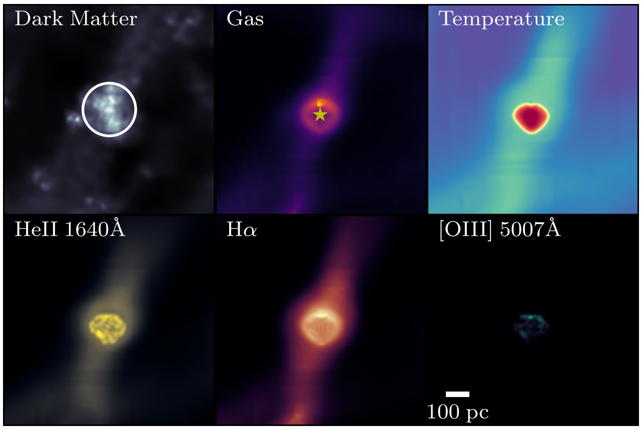

Figure 7. Maps of the dark matter, gas, temperature, He II 1640 Å, H α, and [O III] 5007 Å are shown for a Pop. III SN remnant that had an initial mass of 180.59 M$_\odot$. The circle in the top left panel represents the virial radius of the halo (292 pc) and the yellow star in the top centre panel shows the location of the star particle when the SN exploded.

compared to a Pop. III stellar population. If all haloes that produce Pop. III stars eventually go on to form Pop. II stellar populations, the ratios of time window for detection means that the vast majority of detected systems will be Pop. II.

3.5 Pure line emitters as a signature of Pop. III stars

Due to the nature of our chosen Pop. III IMF, the stars can either end their lives as normal Type-II SN, PISN, or by directly collapsing into black holes. In all three cases, the gas in the host halo will emit for some period of time after the Pop. III star has evolved off the main sequence. In this case, the galaxy may appear to have strong emission lines (and possibly a nebular continuum), but no stellar continuum due to the fact that the star formed in isolation. We refer to these galaxies as PLEs, although similar signatures have been found for active galactic nucleus (e.g. Lintott et al. 2009).

We find two types of PLEs in the simulation: metal-enriched PLEs, which result from a single Pop. III SN, and metal-free PLEs that are generated by the formation of a Pop. III star that subsequently collapses directly into a black hole. SN PLEs will have a spectra of an SN remnant while metal-free PLEs will appear like a fading H II region. Both are labelled in Fig. 5. The two types of PLE have different emission line signatures (i.e. the presence of metals or not), but both seem to have emission lines that fade very fast. The gas density at which the SN explodes as well as the gas distribution (Blondin et al. 1998; Thornton et al. 1998) may impact the rate at which the SN remnant cools; thus the single PISN-driven PLE in our simulation may not be fully representative of the expected parameter space. Nevertheless, detecting these objects may be difficult due to their short-lived nature, but if equivalent widths can be constrained, they may provide an alternative metric for identifying Pop. III systems.

It is important to consider that there may be other types of objects that can be confused with PLEs. For example, a black hole that turns on and off in a pristine or even metal enriched galaxy could potentially show similar features to a PLE. Nakajima & Maiolino (2022) showed that the He II 1640 Å/Ly α ratio (and therefore also He II 1640 Å/H α) is similar between Pop. III stars and direct collapse black holes, peaking at a few per cent. Only the equivalent width of He II 1640 Å could differentiate the two types of sources (when only

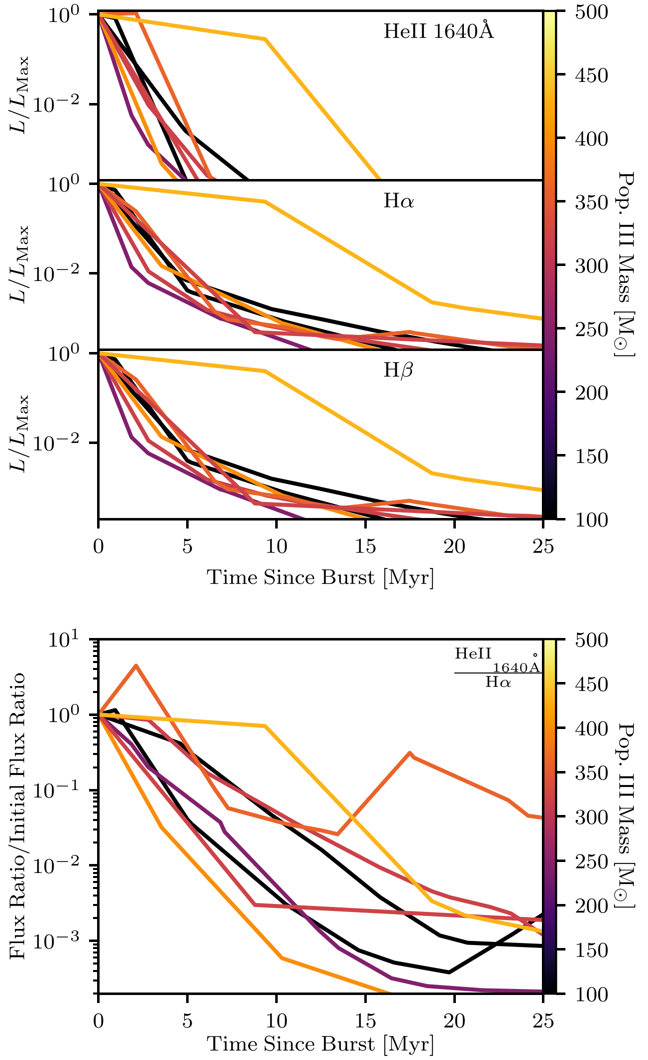

Figure 8. Top: Time evolution of He II 1640 Å, H α, and H β emission normalized to the maximum luminosity of each emission line after the burst as a function of time since the formation of a Pop. III star for eight halos in the simulation. The colour of the line indicates the mass of the Pop. III star that formed during the initial burst. Bottom: Flux ratio of He II 1640 Å to H α normalized by the ratio at the time of the burst. In most cases, the emission line strengths fade within 5 Myr, with He II 1640 Å fading faster than the Balmer emission.

these lines are observed). If the source turns off, the equivalent width cannot be measured. If star formation is very heavily dust obscured than the continuum may not be detectable, but if there is a gas cloud near the star-forming region that is not obscured, this could mimic a PLE. However, we would not expect hard spectral features unless the system contained, for example, X-ray binaries, Wolf–Rayet stars, a black hole, etc. We would not expect this set-up to be confused with our metal-free PLEs unless the nearby gas cloud is also pristine or of very low metallicity.

4 CAVEATS

The primary systematic uncertainties with our work are the choices of Pop. III IMF, main-sequence lifetimes, SED, post-main-sequence behaviour, metal yields, and the transition metallicity between Pop. III and Pop. II star formation. Ideally, we could run more simulations to vary these parameters; however, the computational expense of these simulations poses a severe limitation. Nevertheless, one can speculate how changes to these assumptions will impact our results.

For example, moving to a less top heavy IMF may allow the spectral signatures of Pop. III stars to last much longer due to the extended main-sequence lifetimes. Making the SEDs less or more hard will impact the strength of the He II 1640 Å line with respect to the Balmer lines by making the ratios weaker or stronger, respectively. Depending on whether the Pop. III stars collapse directly to black holes or explode as SN, this could change the time-scale for enrichment. The abundance patterns of the enriched gas will change depending on the ratio of PISN to normal core–collapse SN. Given that our models with the highest SFRs are in good agreement with results from previous CLOUDY models (Inoue 2011; Nakajima & Maiolino 2022), barring the additional scatter due to SFR, galaxy structure, etc., varying these parameters in photoionization models will provide a good estimate for the expected signatures of Pop. III stars.

One of the key uncertainties with our modelling is whether Pop. III stars form in isolation or in large groups. Due to resolution, most Pop. III stars in our work form in isolation; however, higher resolution simulations that better resolve the star formation process show that Pop. III stars can form in binaries or small groups (e.g. Stacy, Bromm & Lee 2016). This could help increase the time period over which He II is bright.

Due to computational expense, we have only run one simulation of the Lagrange region around a single halo. As described earlier, the onset of Pop. III star formation and length of the Pop. III–Pop. II transition will be halo and environment dependent. Nevertheless, we speculate that there will be qualitatively similar behaviour in other similar environments. The galaxies in our simulation are intrinsically faint, but we expect the emission line ratios to hold for any more massive galaxy with similar ISM properties that may be more luminous. More simulations will be required to sample the true diversity of high-redshift galaxies.

5 CONCLUSIONS

We have run a high-resolution cosmological radiation hydrodynamics zoom-in simulation of the region around a dwarf galaxy at $z \geq 10$ with sub-pc resolution to predict the emission line signatures of the Pop. III/Pop. II transition. The simulations are uniquely run with the RAMSES-RTZ code (Katz 2022), which allows us to predict emission line signatures from both primordial species and metals in a fully non-equilibrium manner.

We predict that early metal enrichment from Pop. III stars can quickly increase the mass-weighted metallicity of the gas up to $10^{-4}\,{\rm Z}_\odot$ as measured by O and Fe abundances, which is similar to the results of other simulations (e.g. Wise et al. 2012b). This metallicity floor is enough to initiate the formation of the first generations of Pop. II stars at $z \sim 16.5$. A mixed-mode of Pop. III and Pop. II star formation continues until $z \sim 11$, when the Lagrange region is sufficiently metal enriched enough so that Pop. II star formation dominates the volume.

We calculate emission line luminosities of [O III] 5007 Å, [O II] 3727 Å, H α, H β, and He II 1640 Å and show that even among metal enriched galaxies (i.e. those with $Z \gtrsim 0.01\,{\rm Z}_\odot$), the [O III] 5007 Å/H β ratio can remain below 10^{-2}, consistent with CLOUDY calculations (Inoue 2011; Nakajima & Maiolino 2022), indicating that it will be difficult to identify a truly metal free galaxy with *JWST* due to sensitivity limits. Combining this ratio with He II 1640 Å/H α, we find that there is parameter space with [O III]/H $\beta < 10^{-1.5}$ and He II 1640 Å/H $\alpha > 10^{-0.6}$ that is populated only by galaxies dominated by Pop. III star formation. However, this parameter space is sparsely populated because the He II 1640 Å emission fades very quickly (i.e. within a ∼5 Myr) after the onset of star formation. Hard He II 1640 Å/H α ratios can only be maintained for longer periods of time if multiple Pop. III stars form in sequence or with different masses in the same system, which is rare in our model. Finally, we propose that galaxies with emission lines but no detectable continua (i.e. PLEs) could offer a signature of a Pop. III stars that either subsequently collapsed directly into a black hole (if there are no metal emission lines) or Pop. III stars that exploded via SN (if there are metal emission lines). PLEs are also expected to be short lived, but could represent a further diagnostic of Pop. III star formation if detected. It is unlikely that we will be able to robustly detect a PLE with *JWST* because one would have to conclusively rule out the presence of a faint continuum which can have very low S/N in faint targets (e.g. Cameron et al. 2023).

In summary, *JWST* will provide an exciting probe of star formation and possibly even Pop. III star formation in the early Universe. However, our work demonstrates that there are significant challenges in robustly identifying a Pop. III stellar population that should be taken into consideration when analysing upcoming *JWST* data.

ACKNOWLEDGEMENTS

HK thanks Aayush Saxena, Martin Rey, Alex Cameron, Eric Andersson, Oscar Agertz, and Girish Kulkarni. This project has received funding from the European Research Council (ERC) under the European Union's Horizon 2020 research and innovation programme (grant agreement no. 693024). TK was supported by the National Research Foundation of Korea (NRF) grant funded by the Korea government (nos 2020R1C1C1007079 and 2022R1A6A1A03053472). RSE acknowledges funding from the European Research Council under the European Union Horizon 2020 research and innovation programme (grant agreement no. 669253). Some of this work used the DiRAC@Durham facility managed by the Institute for Computational Cosmology on behalf of the STFC DiRAC HPC Facility (www.dirac.ac.uk). The equipment was funded by BEIS capital funding via STFC capital grants ST/P002293/1, ST/R002371/1, and ST/S002502/1, Durham University and STFC operations grant ST/R000832/1. Some of this work was performed using the DiRAC Data Intensive service at Leicester, operated by the University of Leicester IT Services, which forms part of the STFC DiRAC HPC Facility (www.dirac.ac.uk). The equipment was funded by BEIS capital funding via STFC capital grants ST/K000373/1 and ST/R002363/1 and STFC DiRAC Operations grant ST/R001014/1. DiRAC is part of the National e-Infrastructure.

DATA AVAILABILITY

The data underlying this article will be shared on reasonable request to the corresponding author.

REFERENCES

Abel T., Bryan G. L., Norman M. L., 2002, Science, 295, 93
Agertz O., Kravtsov A. V., Leitner S. N., Gnedin N. Y., 2013, ApJ, 770, 25
Beers T. C., Christlieb N., 2005, ARA&A, 43, 531
Blondin J. M., Wright E. B., Borkowski K. J., Reynolds S. P., 1998, ApJ, 500, 342
Bromm V., Coppi P. S., Larson R. B., 2002, ApJ, 564, 23
Bryan G. L., Norman M. L., 1998, ApJ, 495, 80
Cameron A. J. et al., 2023, preprint (arXiv:2302.04298)
Carilli C. L., Murphy E. J., Ferrara A., Dayal P., 2018, preprint (arXiv:1810.07536)
Erb D. K., Pettini M., Shapley A. E., Steidel C. C., Law D. R., Reddy N. A., 2010, ApJ, 719, 1168
Federrath C., Klessen R. S., 2012, ApJ, 761, 156
Ferland G. J. et al., 2017, Rev. Mex. Astron. Astrofis., 53, 385
Frebel A., Johnson J. L., Bromm V., 2007, MNRAS, 380, L40
Gardner J. P. et al., 2006, Space Sci. Rev., 123, 485
Gill S. P. D., Knebe A., Gibson B. K., 2004, MNRAS, 351, 399
Glover S. C. O., Clark P. C., 2012, MNRAS, 426, 377
Greif T. H., Springel V., White S. D. M., Glover S. C. O., Clark P. C., Smith R. J., Klessen R. S., Bromm V., 2011, ApJ, 737, 75
Grisdale K., Thatte N., Devriendt J., Pereira-Santaella M., Slyz A., Kimm T., Dubois Y., Yi S. K., 2021, MNRAS, 501, 5517
Gunn J. E., Peterson B. A., 1965, ApJ, 142, 1633
Hahn O., Abel T., 2011, MNRAS, 415, 2101
Heger A., Woosley S. E., 2002, ApJ, 567, 532
Hirano S., Hosokawa T., Yoshida N., Umeda H., Omukai K., Chiaki G., Yorke H. W., 2014, ApJ, 781, 60
Hosokawa T., Hirano S., Kuiper R., Yorke H. W., Omukai K., Yoshida N., 2016, ApJ, 824, 119
Inoue A. K., 2011, MNRAS, 415, 2920
Inoue A. K., Shimizu I., Iwata I., Tanaka M., 2014, MNRAS, 442, 1805
Izotov Y. I., Guseva N. G., Fricke K. J., Henkel C., 2019, A&A, 623, A40
Jeon M., Bromm V., 2019, MNRAS, 485, 5939
Karlsson T., Bromm V., Bland-Hawthorn J., 2013, Rev. Mod. Phys., 85, 809
Katz H., 2022, MNRAS, 512, 348
Katz H., Kimm T., Sijacki D., Haehnelt M. G., 2017, MNRAS, 468, 4831
Katz H. et al., 2022, MNRAS, 515, 4265
Kimm T., Cen R., Devriendt J., Dubois Y., Slyz A., 2015, MNRAS, 451, 2900
Kimm T., Katz H., Haehnelt M., Rosdahl J., Devriendt J., Slyz A., 2017, MNRAS, 466, 4826
Knollmann S. R., Knebe A., 2009, ApJS, 182, 608
Kroupa P., 2001, MNRAS, 322, 231
Lazar A., Bromm V., 2022, MNRAS, 511, 2505
Levermore C. D., 1984, J. Quant. Spectrosc. Radiat. Transfer, 31, 149
Lintott C. J. et al., 2009, MNRAS, 399, 129
Luridiana V., Morisset C., Shaw R. A., 2015, A&A, 573, A42
Maiolino R., Mannucci F., 2019, A&AR, 27, 3
Nakajima K., Maiolino R., 2022, MNRAS, 513, 5134
Nelson R. P., Langer W. D., 1997, ApJ, 482, 796
Nomoto K., Tominaga N., Umeda H., Kobayashi C., Maeda K., 2006, Nucl. Phys. A, 777, 424
Oh S. P., Haiman Z., Rees M. J., 2001, ApJ, 553, 73
Oppenheimer B. D., Schaye J., 2013, MNRAS, 434, 1043
O'Shea B. W., Norman M. L., 2007, ApJ, 654, 66
Padoan P., Nordlund Å., 2011, ApJ, 730, 40
Pawlik A. H., Milosavljević M., Bromm V., 2011, ApJ, 731, 54
Pignatari M. et al., 2016, ApJS, 225, 24
Planck Collaboration VI, 2020, A&A, 641, A6
Portinari L., Chiosi C., Bressan A., 1998, A&A, 334, 505
Raiter A., Schaerer D., Fosbury R. A. E., 2010, A&A, 523, A64
Raiteri C. M., Villata M., Navarro J. F., 1996, A&A, 315, 105
Rémy-Ruyer A. et al., 2014, A&A, 563, A31
Rosdahl J., Teyssier R., 2015, MNRAS, 449, 4380
Rosdahl J., Blaizot J., Aubert D., Stranex T., Teyssier R., 2013, MNRAS, 436, 2188
Rydberg C.-E., Zackrisson E., Lundqvist P., Scott P., 2013, MNRAS, 429, 3658
Schaerer D., 2002, A&A, 382, 28
Schaerer D., 2003, A&A, 397, 527
Schaerer D., Fragos T., Izotov Y. I., 2019, A&A, 622, L10
Schauer A. T. P., Drory N., Bromm V., 2020, ApJ, 904, 145
Schmidt M., 1959, ApJ, 129, 243
Seitenzahl I. R. et al., 2013, MNRAS, 429, 1156

Sobral D., Matthee J., Darvish B., Schaerer D., Mobasher B., Röttgering H. J. A., Santos S., Hemmati S., 2015, ApJ, 808, 139
Stacy A., Greif T. H., Bromm V., 2010, MNRAS, 403, 45
Stacy A., Bromm V., Lee A. T., 2016, MNRAS, 462, 1307
Stanway E. R., Eldridge J. J., 2018, MNRAS, 479, 75
Stiavelli M., Trenti M., 2010, ApJ, 716, L190
Teyssier R., 2002, A&A, 385, 337
Thornton K., Gaudlitz M., Janka H. T., Steinmetz M., 1998, ApJ, 500, 95
Tumlinson J., Giroux M. L., Shull J. M., 2001, ApJ, 550, L1
Vanzella E. et al., 2020, MNRAS, 494, L81
Vikaeus A., Zackrisson E., Schaerer D., Visbal E., Fransson E., Malhotra S., Rhoads J., Sahlén M., 2022, MNRAS, 512, 3030
Welch B. et al., 2022, Nature, 603, 815
Wise J. H., Abel T., Turk M. J., Norman M. L., Smith B. D., 2012a, MNRAS, 427, 311
Wise J. H., Turk M. J., Norman M. L., Abel T., 2012b, ApJ, 745, 50
Woosley S. E., Weaver T. A., 1995, ApJS, 101, 181
Xu H., Norman M. L., O'Shea B. W., Wise J. H., 2016, ApJ, 823, 140
Yang H. et al., 2017a, ApJ, 844, 171
Yang H., Malhotra S., Rhoads J. E., Wang J., 2017b, ApJ, 847, 38
Zackrisson E., Rydberg C.-E., Schaerer D., Östlin G., Tuli M., 2011, ApJ, 740, 13
Zackrisson E. et al., 2012, MNRAS, 427, 2212

This paper has been typeset from a TEX/LATEX file prepared by the author.